Chemosphere 316 (2023) 137855

Contents lists available at ScienceDirect

Chemosphere

journal homepage: www.elsevier.com/locate/chemosphere

Anthropogenic activity and millennial climate variability affect Holocene mercury deposition of an alpine wetland near the largest mercury mine in China

Haijun Peng [a,f,*], Yimeng Rong [a,b,e], Di Chen [b,e], Ruiyang Sun [a,b,e], Jie Huang [c], Hanwei Ding [a,e], Carolina Olid [d], Haiyu Yan [a]

[a] State Key Laboratory of Environmental Geochemistry, Institute of Geochemistry, Chinese Academy of Sciences, Guiyang, 550081, China
[b] State Key Laboratory of Ore Deposit Geochemistry, Institute of Geochemistry, Chinese Academy of Sciences, Guiyang, 550081, China
[c] Key Laboratory of Tibetan Environment Changes and Land Surface Processes, Institute of Tibetan Plateau Research, Chinese Academy of Sciences, Beijing, 100101, China
[d] UB-Geomodels Research Institute, Departament de Dinàmica de la Terra i l'Oceà, Facultat de Ciències de la Terra, Universitat de Barcelona, Barcelona, 08028, Spain
[e] University of Chinese Academy of Sciences, Beijing, 100049, China
[f] CAS Center for Excellence in Quaternary Science and Global Change, Xi'an, 710061, China

HIGHLIGHTS

- Hg mining activities in the Wanshan Hg Mine area might have started 2500 years ago.
- Pre-industrial Hg accumulation rate in Jiulongchi experienced 4–8 times variations.
- Two Hg_{influx} peaks were detected in wetland archives across Northern Hemisphere.
- Intensified Hg accumulation in lake records was ascribed to millennial abrupt climatic changes.

GRAPHICAL ABSTRACT

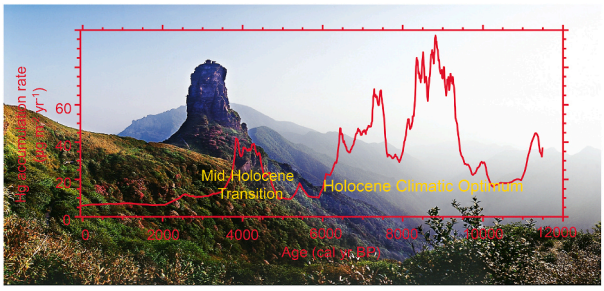

ARTICLE INFO

Handling Editor: Milena Horvat

Keywords:
Mercury
Atmospheric deposition
Holocene
Climate change
Wanshan mercury mine

ABSTRACT

Mercury (Hg) is a potentially toxic element that can be transported globally through the atmosphere, once deposited in the environment, has strong bioaccumulation and extreme toxicity in food webs, especially in wetland ecosystems. Anthropogenic Hg emissions have enhanced Hg deposition by 3–5 times since the industrial revolution, and the mining and smelting of Hg ore are important emission sources. However, the dynamics in Hg deposition around the largest Hg mine in China before the industrial revolution and their driving forces remain poorly explored. Here we reconstruct the atmospheric Hg depositional fluxes (named here Hg influx (Hg_{influx})) during the Holocene using a 450-cm alpine wetland sediment core taken from the Jiulongchi wetland, which is only 65 km to the Wanshan Mercury Mine. Our record shows an abrupt rapid increase in Hg concentration since 2500 cal yr BP, suggesting that Hg mining in southwest China may have started before the establishment of the Qin dynasty. Two major Hg_{influx} peaks were found during the periods 10,000–6000 and 6000 - 3800 cal yr BP, with an increase in Hg deposition by a factor of 4–8. These two peaks are also found in other terrestrial archives from several sites across the Northern Hemisphere. We speculate that critical millennial-scale climate changes, i.

* Corresponding author. State Key Laboratory of Environmental Geochemistry, Institute of Geochemistry, Chinese Academy of Sciences, Guiyang, 550081, China.
E-mail address: penghaijun@mail.gyig.ac.cn (H. Peng).

https://doi.org/10.1016/j.chemosphere.2023.137855
Received 10 November 2022; Received in revised form 9 January 2023; Accepted 11 January 2023
Available online 12 January 2023

e., the Holocene Climatic Optimum (HCO) and the Mid-Holocene Transition (MHT), were the potential triggers of these two Hg_{influx} peaks. This study highlights the importance of climatic variability and local Hg mining in controlling atmospheric Hg deposition during the Holocene.

1. Introduction

Mercury (Hg) is a globally distributed pollutant, which attracts the world's attention due to its long-range transport in the atmosphere, strong biomagnification in the food chain, and deleterious impact on ecosystem health (Selin, 2009). Both natural and anthropogenic activities emit large amounts of Hg into the atmosphere, mainly in the form of gaseous Hg^0. The long residence time of gaseous Hg^0 (~1 year) in the atmosphere allows for its global dispersion before being deposited in terrestrial and aquatic ecosystems via wet and dry deposition pathways (Obrist et al., 2018). The Hg deposited into aquatic ecosystems can be methylated via microbial activities and then form methylmercury (MeHg), a neurotoxin that can bioaccumulate up to 10^6 times in food webs (Grégoire et al., 2018; Obrist et al., 2018). Lakes serve as an important sink for Hg in aquatic ecosystems by receiving Hg through atmospheric deposition and runoff of soil-bounded Hg species (Pompeani et al., 2018). Thus, significant Hg accumulation has occurred in aquatic food chains and high fish MeHg levels found in remote lakes, such as those in Northern Europe and North America (Lepak et al., 2020; Wang et al., 2021).

Sedimentary archives, such as lake sediments and peat cores, are used to quantify long-term (centennial to millennial time scales) changes in terrestrial Hg cycling (Cooke et al., 2020). The amount of Hg entering the lakes is normally quantified by Hg influx (Hg_{influx}, μg m^{-2} yr^{-1}), which is calculated by multiplying sediment Hg concentration (μg g^{-1}) by sediment accumulation rate (g m^{-2} yr^{-1}). Sedimentary records in remote lakes showed an increase in Hg_{influx} by a factor of 3–5 since the onset of global industrialization in the 1800s (Lamborg et al., 2002; Pompeani et al., 2018; Lepak et al., 2020; Neupane et al., 2022). As sediment accumulation rates in these lakes were almost constant during this period, the increase in Hg_{influx} has been ascribed to an increase of Hg concentrations in sediments, due to a globally increased anthropogenic Hg input to the lakes. In recent decades, the amount of Hg emitted by anthropogenic activities (~3400 tons yr^{-1}) has caught up or overwhelmed that emitted from natural activities (Selin, 2009).

In geological history, when anthropogenic Hg emission was not significant, Hg cycling in the environment was governed by the degassing of Hg through volcanisms, generally at lower rates ranging from 75 to 700 tons yr^{-1} (Selin, 2009). However, large igneous provinces (LIPs) eruptions often occurred and could emit massive amounts of Hg into the atmosphere (Grasby et al., 2019). For example, Hg emissions from the Siberian Traps LIP event (~252 Ma) was estimated to be ~10, 000 tons yr^{-1}, which is ~3 times higher than modern anthropogenic emission rates (Grasby et al., 2015). The extreme loading of volcanic Hg during LIPs eruptions has been revealed by significant high Hg concentration peaks in ancient sedimentary rocks (Grasby et al., 2019). However, when LIPs were absent, large variations of Hg concentrations remained observed in some sedimentary records, especially during the Holocene epoch (Jacobson et al., 2012; Hermanns and Biester, 2013; Pompeani et al., 2018). In this case, Hg_{influx} may not have been governed by volcanic Hg emission and deposition. In contrast, global environmental changes (e.g., changes in precipitation rates, sedimentation rates and weathering intensity) may trigger the variable accumulation rates of Hg in the sediments.

While the impact of enhanced Hg loading on ecosystems is of major concern globally in recent decades (Obrist et al., 2018), our understanding of the effects of global environmental changes on the Hg cycle over millennial time scales is minimal (Cooke et al., 2020; Li et al., 2020b). The Holocene, which started ~11.6 kyr ago, has undergone significant changes in global temperature, precipitation, and sea level (DahlJensen et al., 1998; Kaufman et al., 2004) that altered atmospheric circulation, landscapes, and soil erosion. It has been widely reported that large variations in Hg_{influx} during the Holocene were observed in lake records worldwide (Hermanns and Biester, 2013; Pompeani et al., 2018; Schütze et al., 2018; Pan et al., 2020). Despite that early anthropogenic Hg mining (Martínez-Cortizas et al., 1999; Beal et al., 2013) and volcanic eruptions (Roos-Barraclough et al., 2002; Beal et al., 2014) could cause abrupt variations in Hg accumulations in sediments on a local spatial scale, the impact of the Holocene environmental changes on Hg accumulation in lake sediments remains unclear.

Wanshan Hg mine, the largest Hg mine in China and the 3rd largest in the world, has a long history of Hg exploitation and smelting (Zhang et al., 2010; Yin et al., 2017). Though the Hg speciation and isotopes and their pollution risks to local residents and animals have been well investigated (Zhang et al., 2010; Yin et al., 2013, 2017), little is known about the history of the long-term Hg mining in the Wanshan region and the baseline environment Hg concentration before the mining. Modern measurements have demonstrated that *the volatile* atmospheric Hg tends to be deposited in montane regions due to their cold environments and unique orographic conditions, which is known as the "mountain trapping effect" of Hg (Zhang et al., 2013). Thus, it is considered that alpine lakes are ideal archives of historical atmospheric Hg deposition studies (Yin et al., 2016). In this study, we examine the impact of local Hg mining activities and millennial environmental changes (e.g., temperature, precipitation, and sedimentations) on the Holocene Hg deposition in the Jiulongchi alpine wetland, located very close to the highest peak (Fanjingshan Mountain) of the Wuling Mountains in southeast China and only 65 km away from the Wanshan Hg mine. The specific objectives of this study are (1) to reconstruct the dynamics in the Hg deposition in southwest China during the Holocene, (2) to access the effect of historical local Hg mining on Hg accumulation in the alpine lake, and (3) to investigate the links between centennial-millennial timescale climate changes and the Hg deposition in the Northern Hemisphere.

2. Materials and method

2.1. Study site

Jiulongchi wetland (108°41′33″E, 27°53′57″ N, 2048 *m* a.s.l.) is a small, drained cirque lake (width: ~30 *m*; length: ~110 *m*) located near the Golden Summit of the Fanjingshan Mountain, Guizhou province, southwest China (Fig. 1). Fanjingshan Mountain is at the west end of the Jiangnan orogen (Xiong et al., 2013), where developed lots of cinnabar ores, such as Wanshan, Lanmuchang, and Wuchuan Hg mines in Guizhou Province, Fenghuang, Xinhuang, and Baojing Hg mines in Hunan Province (Li et al., 2013; Pan et al., 2020). Jiulongchi is only 100 km to the Wuchuan Hg Mine and 65 km to the Wanshan Hg Mine (Fig. 1b). The latter is the largest Hg mine in China and the world's third-largest, and its mining history can be traced back to more than 2000 years ago (Zhang et al., 2010).

The Fanjingshan Mountain region is characterized by a subtropical monsoon climate with hot and humid summer that is influenced by the Asian summer monsoon. The annual precipitation and mean annual temperature are about 1100–2600 mm and 6–17 °C, respectively (Gao et al., 2019). The bedrocks surrounding Jiulongchi are metamorphic diabase, tuff, slate, and sandstone in a Precambrian stratum of the Fanjingshan Group, which were formed more than 800 million years ago (Xiong et al., 2013). The surrounding topography of the Jiulongchi wetland is steep, with no river or stream input (Fig. 1 b and d). Water and sediment of the Jiulongchi are mainly originated from natural

precipitation and local soil erosion. The altitude of the peak and foot of Fanjingshan Mountain are 2572 *m* and 500 *m*, respectively. Benefiting from the large altitudinal gradients, vegetation cover in this region has a unique vertical zonal distribution pattern. The vegetation composition is dominated by broad-leaf deciduous trees (Liao and Ren, 2015; Gao et al., 2019).

2.2. Sample collection and X-ray fluorescence (XRF) scanning

Two parallel cores (FJ19A and FJ19B), 30 cm apart from each other, were collected using a Russian peat corer from the center of Jiulongchi (Fig. 1d) in April 2019. The total length of the cores was 450 cm, and both cores shared the same stratigraphical sequence. To minimize compaction during transport, the collected samples were packed in 50 cm-long polymethyl methacrylate half-cylinder tubes and wrapped with plastic film. XRF core scanning was then carried out on the FJ19A core by using a standard Multi-Sensor Core Logger (MSCLs, Geotek Ltd., UK) at the Nanjing Institute of Geography and Limnology, Chinese Academy of Sciences. The MSCLs firstly took high-resolution (1 cm interval) photos (Fig. 2a) and then measured brightness (L*), redness (a*), yellowness (b*) by using a spectrophotometer, and element concentration by using a XRF logger. Element concentrations were measured at a voltage of 10 kV for 15–20 s and the intensities are expressed as counts per second (cps). Because of rough surfaces or measuring time shorter than 15 s, 17 out of the 450 XRF measurements were discarded.

2.3. Chronology and elemental analysis

Collected samples were stored in a cold room (4 °C) at the Institute of Geochemistry, Chinese Academy of Sciences (IGCAS). The cores were sliced into 1 cm sub-samples and stored in self-sealed plastic bags. In the meantime, plant residues (terrestrial macrofossils) were selected for dating. Bulk samples were also extracted for dating when there was not enough plant material for the analysis. A total of 25 samples from 23 depths of the FJ19A core were selected for building the chronology (Table 1). The AMS ^{14}C measurements were conducted at Beta Analytic. The chronological age was calibrated by BetaCal3.21 using the INTAL13 dataset (Reimer et al., 2013). The chronology was established by the Bayesian age-depth model in the Bacon R package based on the calibrated AMS ^{14}C dates (Fig. 2b) (Blaauw and Christen, 2011).

All 1-cm slices of the 450-cm FJ19B core were weighted and then freeze-dried to obtain water content and bulk density. Dried samples were ground using an agate mortar and homogenized for further analysis. Total Hg (THg) concentrations of all 450 samples (FJ19B) were analyzed by a direct mercury analyzer (DMA-80, Milestone Inc., Italy). TOC concentrations were measured following the Walkley-Black procedure (Walkley, 1947). Measurements of a standard reference material (GSS-5, soil) yielded Hg recoveries of 90–110%, and the relative

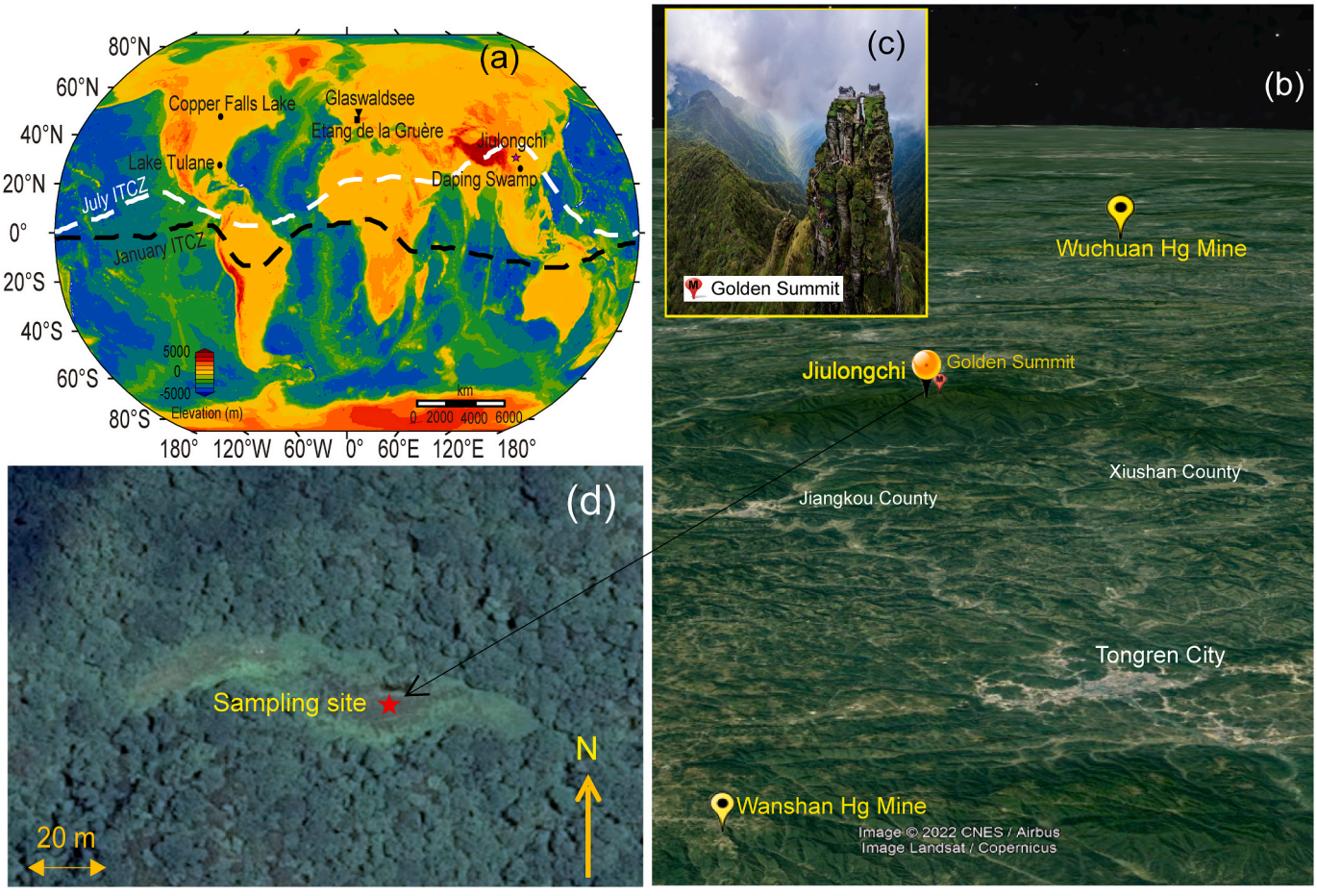

Fig. 1. Maps showing the locations of the Jiulongchi wetland and previously studied Holocene Hg records. (a) Locations of Copper Falls Lake (Pompeani et al., 2018), Daping Swamp (Pan et al., 2020), Lake Tulane (Jacobson et al., 2012), Glaswaldsee (Schütze et al., 2018), Etang de la Gruère peat bog (Roos-Barraclough et al., 2002), and Jiulongchi (this study, marked with a red pentagram). Dashed white and black lines show the modern position of the Intertropical Convergence Zone (ITCZ) in July and January, respectively (Cheng et al., 2012). Terrain data was retrieved from NOAA Etopo5 (https://www.ngdc.noaa.gov/mgg/global/etopo5.HTML). (b) Bird view of Fanjingshan Mountain region with the locations of the sampling site, surrounding cities, and nearby Hg mines marked. (c) The physical picture of the Golden Summit of Fanjingshan shows the topography that surrounds the Jiulongchi wetland. (d) Aerial photo of Jiulongchi wetland with a red pentagram showing the coring spot. (For interpretation of the references to color in this figure legend, the reader is referred to the Web version of this article.)

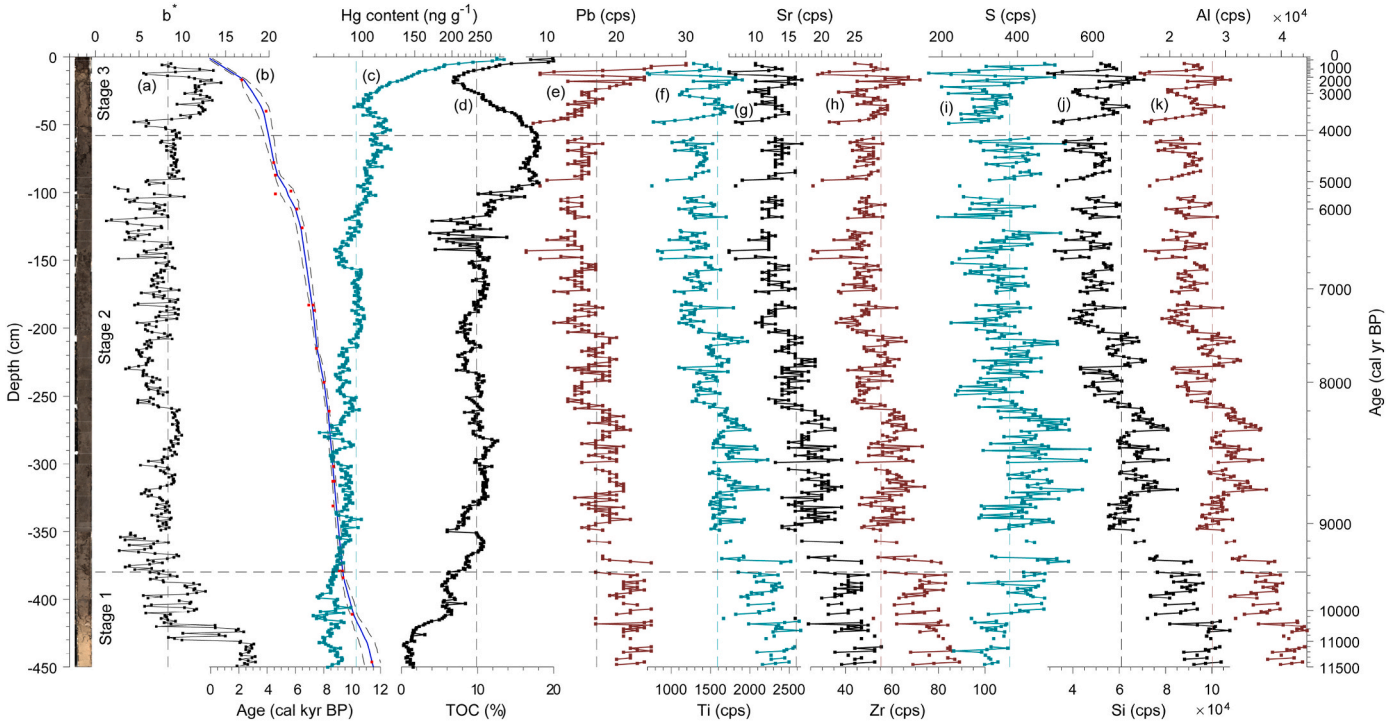

Fig. 2. (a) Lithology and yellowness (b*) of the FJ19A core, and its (b) age-depth model (blue line showing the mean age and with dashed blue lines represent the associated uncertainties, and solid red squares showing the age control points), (c) Hg concentration (note that the x-axis is a log scale), and (d) TOC, and (e), (f), (g), (h), (i), (j), and (k) are Pb, Ti, Sr, Zr, S, Si, and Al concentrations measured by the XRF detector in the MSCLs, respectively. Vertical dashed lines were the mean values of the measurements. (For interpretation of the references to color in this figure legend, the reader is referred to the Web version of this article.)

Table 1
Results of ^{14}C analyses of FJ19A from the Jiulongchi wetland.

Sample ID	Lab code	Depth (cm)	$\delta^{13}C$ (‰, VPDB)	^{14}C age (yr BP)	Dating material	Calibrated age range (cal yr BP)
FJ19A-1-17	530997	17	−28.7	2230 ± 30	Bulk sample	2277–2153
FJ19A-1-40	530998	40	−29	3630 ± 30	Bulk sample	3994–3855
FJ19A-2-28	529484	78	−25.5	3970 ± 30	Seed	4524–4401
FJ19A-2-37	529486	87	−26.2	4080 ± 30	Seed	4648–4514
FJ19A-2-49	530999	99	−29.7	4960 ± 30	Bulk sample	5742–5609
FJ19A-3-1	529485	101	−24.4	4080 ± 30	Seed	4648–4514
FJ19A-3-12	531000	112	−30.3	5320 ± 30	Bulk sample	6192–5996
FJ19A-3-26	531001	126	−30.8	5680 ± 30	Bulk sample	6538–6402
FJ19A-4-33-1	531002	183	−31	6330 ± 30	Bulk sample	7318–7173
FJ19A-4-33-2	529491	183	−27.1	6080 ± 30	Bark and leaf	7014–6853
FJ19A-4-37	531003	187	−30.2	6400 ± 30	Bulk sample	7418–7270
FJ19A-5-15	529493	215	−29.3	6590 ± 30	Bulk sample	7520–7431
FJ19A-5-40	529494	240	−29.3	7210 ± 30	Bulk sample	8063–7958
FJ19A-6-11-2	531004	261	−13.2	7550 ± 30	Bulk sample	8410–8333
FJ19A-7-2	529495	302	−27.4	7860 ± 30	Seed	8763–8583
FJ19A-7-13	531005	313	−30.3	7930 ± 30	Bulk sample	8811–8635
FJ19A-7-13-1	529498	313	−27.3	7840 ± 30	Leaf	8715–8547
FJ19A-7-31	529499	331	−28.3	7850 ± 30	Bark and leaf	8722–8554
FJ19A-8-24	529500	374	−26.9	8220 ± 30	Bark	9291–9082
FJ19A-8-29	529501	379	−28.8	8110 ± 30	Leaf	9122–8997
FJ19A-8-29-1	529502	379	−27.3	8290 ± 30	Branch	9424–9202
FJ19A-8-34	529503	384	−25.2	8330 ± 30	Seed	9447–9272
FJ19A-9-11	531006	411	−28.6	8920 ± 30	Bulk sample	10,091–9917
FJ19A-9-33	529505	433	−26.3	10,250 ± 30	Bulk sample	12,130–11,920
FJ19A-9-46	531007	446	−27.3	9970 ± 40	Bulk sample	11,509–11,259

standard deviations of sample duplicates were less than 10%. To estimate Hg accumulation rates (Hg_{influx}), we used the equation used in previous studies (Roos-Barraclough et al., 2002; Pan et al., 2020).

$$Hg_{influx} = Hg_{conc.} \times BD \times SAR$$

Where $Hg_{conc.}$ Is the Hg concentration (μg g^{-1}) of a given depth, BD is bulk density (g cm^{-3}), and SAR is sedimentation accumulation rate (cm yr^{-1}). SAR was determined based on the ages derived from the Bacon age-depth model.

3. Results

3.1. Physical property and stratigraphy

The lithological record of the 450 cm long FJ19A core can be divided into three subunits based on soil structure, yellowness (b*), and TOC (Fig. 2a, c, and d). Stage 1: from −450 cm to −380 cm depth, yellow-brownish coarse-fine grained sandy sediments, with b*, TOC, THg, and SAR being (mean ± std) 10.35 ± 2.36, 3.87 ± 2.44%, 78.85 ± 4.33 ng g^{-1}, and 0.037 ± 0.013 cm yr^{-1}, respectively; Stage 2: from −379 cm to −61 cm depth, brown-blackish fine grained sandy sediments, with b*, TOC, THg, and SAR being 7.16 ± 1.80, 10.63 ± 2.79%, 91.81 ± 8.61 ng g^{-1}, and 0.080 ± 0.032 cm yr^{-1}, respectively; Stage 3: from −60 cm to 0 cm depth, brownish fine grained sandy sediments, with b*, TOC, THg, and SAR being 11.93 ± 4.22, 10.35 ± 2.36, 12.76 ± 3.84%, 133.18 ± 45.67 ng g^{-1}, and 0.024 ± 0.018 cm yr^{-1}, respectively. Based on the age-depth model, the sedimentation rate during Stage 2 was stable and higher than during Stage 1 and Stage 3 (Fig. 2b). The average time resolution of the 450-cm long record is about 26 yr per cm, which is high enough to investigate centennial to millennial scale environmental and climate variations.

3.2. Geochemical characteristics

Ti, Sr, and Zr have a similar general variation trend with higher content in Stage 1, then generally decreasing during Stage 2 and increasing a bit in Stage 3 (Fig. 2 f, g, and h). While the fluctuations in Si and Al concentrations are much alike, with high concentrations in Stage 1, generally decreasing in Stage 2 and then increasing in Stage 3 (Fig. 2 j and k). Hg concentration, TOC and S concentration display a stepwise increase in Stage 1 (Fig. 2 c, d, and j), Pb, Ti, Sr, and Zr slightly decreased while Si and Al decreased about 50% compared to the section from −450 to −430 cm depth (Fig. 2 e, f, g, h, j, and k). Si, Al, and S exhibited significant variability while the variations in Hg concentration, TOC, and b* are more stable during Stage 2. Besides, more plant macrofossils are observed during this stage. During Stage 3, the sediments are lighter and yellower. While sedimentation rate decreased dramatically, especially for the last 2200 years. This indicates that Jiulongchi lake has started to vanish, and fewer sediments were deposited since then. During the last 4000 years, Hg concentration has increased from 95 to more than 290 ng g^{-1}. While Pb and S showed the same general pattern, increasing from 10 to 30 cps and 200–500 cps, respectively.

The ^{14}C ages of the bulk samples and plant residues indicate that sedimentation at Jiulongchi initiated at ~11,500 yr BP, which is also the beginning of the Holocene (Table 1). The AMS^{14}C dates showed a general increase in age with the increase in depth (Fig. 2b and Table 1). However, the sample from −433 cm depth is slightly older than the sample from −446 cm depth. This could be attributed to the diachronous effect that younger plants rooted in the older stratum. Besides, we dated 3 sets of samples from the same depth (−183 cm, −313 cm, and −379 cm depth) using different dating materials. Bulk samples are always a bit older than plant macrofossil samples and leaf sample is younger than branch sample. The results have been reported in our previous study (Rong et al., 2021).

4. Discussion

4.1. The effect of anthropogenic activities on Hg deposition

The mining and smelting of cinnabar, which is commonly used in pigments and traditional medicines, can be traced back thousands of years ago and has played an important role in changing the historical local Hg deposition (Martínez-Cortizas et al., 1999; Ernst, 2002). Total Hg (THg) in peat or lake sediment has been widely used as a proxy of ancient anthropogenic activities (Martínez-Cortizas et al., 1999; Li et al., 2016; Pompeani et al., 2018). Despite the sedimentation rate during the last 4000 years (top 40 cm) is relatively low (Fig. 3b). An abrupt increase in THg accompanied by rapid increases in also Pb and S concentration starting from 2500 cal yr BP is clearly observed, with Hg concentration increasing from around 130 to 300 ng g^{-1} and Pb concentration increased more than 2 times (Fig. 3a; Fig. 2 c, e, and i). Though there is only one dating control point from the FJ19B core at the depth of 17 cm (2277–2153 cal yr BP) (Table 1). Two AMS^{14}C dates (425 ± 111 and 2815 ± 79 cal yr BP at the depth of −2.5 and −27.5 cm, respectively) from the JL15 core (Gao et al., 2019), which was taken at a spot just a few meters from the FJ19B core, can be used to constrain our chronology result. While −2.5 and −27.5 cm depth in the FJ19B core corresponds to 820 ± 195 and 3008 ± 551 cal yr BP, respectively. This shows that the two sets of age-depth models are comparable, and our age-depth model of the last 3000 years is reliable. It is then suggested that the mining of Hg in this region might have started at the age of around 2500 cal yr BP, which is about 300 years older than the establishment of the Qin dynasty. This shows that the mining of Hg ore in southwest China also has a long history as the Almadén Hg mine in Spain (Díez et al., 2011), where the Hg mining history can be traced back to 2500 cal yr BP (Martínez-Cortizas et al., 1999). In addition, the decrease in Hg concentration in the last sample (Fig. 3a) could be attributed to the shut-down of the Wanshan Hg mine in the early 2000. However, we suggest that evidence from archaeology or Hg isotopes is still needed to disentangle whether the increase is caused by enhanced anthropogenic emissions from the Wanshan Hg mine or is just fluctuations caused by the drying of the wetland.

Other than sediment THg and THg/TOC, Hg_{influx} has also been widely used as an indicator of Hg accumulation in lakes (Pompeani et al., 2018; Cooke et al., 2020; Li et al., 2020a; Pan et al., 2020). For our study core, the general variation trend in Hg_{influx} was accompanied by the parallel fluctuations in the C accumulation rate. Throughout the core, the variations of Hg_{influx} and C accumulation rate do not match with variations of THg concentrations, but mimic those of sedimentation rates, suggesting that Hg accumulation is mainly driven by sedimentation rate (Fig. 3b, c, and d), rather than sediment THg. A significant positive correlation can be observed between Hg_{influx} and sedimentation rates ($R^2 = 0.95$, $p < 0.001$), this suggests that Hg accumulation at Jiulongchi is driven by sedimentation processes. This finding is different from the Hg_{influx} peaks observed in remote lakes since global industrialization (Lamborg et al., 2002; Lepak et al., 2020), when sedimentation accumulation rates did not change much but extensive anthropogenic activities had significantly increased sediment Hg concentrations through atmospheric deposition.

During the last 2200 years, only 16 cm of sediment was deposited in Jiulongchi. Such low sedimentation rates (0.0065 cm yr^{-1}) (Fig. 3a and b) could lead to large uncertainties in the estimated Hg_{influx} due to the low temporal resolution of the record. To avoid overinterpretation due to such uncertainties, Hg_{influx} values for the period since 2200 cal yr BP are not discussed here. Interestingly, Hg_{influx} showed two peaks during 10,000–6000 cal yr BP (Peak I) and 6000 - 3800 cal yr BP (Peak II), with the values range from 40 to 100 and 20–40 μg m^{-2} yr^{-1}, respectively. These Hg_{influx} are comparable with or even greater than modern anthropogenic Hg_{influx} found in Chinese lake record and many sites over the world (range from 5 to 50 μg m^{-2} yr^{-1}) (Drevnick et al., 2016; Cooke et al., 2020; Li et al., 2020a; Pan et al., 2020). These large variations in the Hg_{influx} (up to ~10 times' change) before the industrial period imply that anthropogenic activities were not the sole cause of extensive variations in Hg accumulation in lakes during the Holocene. This demonstrates that sedimentation rate should be taken into consideration to better quantify the discrepancies between modern and preindustrial Hg depositions into lakes, as anthropogenic activities are found to be a geological force that increased lake sedimentation during the last 4000 years (Jenny et al., 2019).

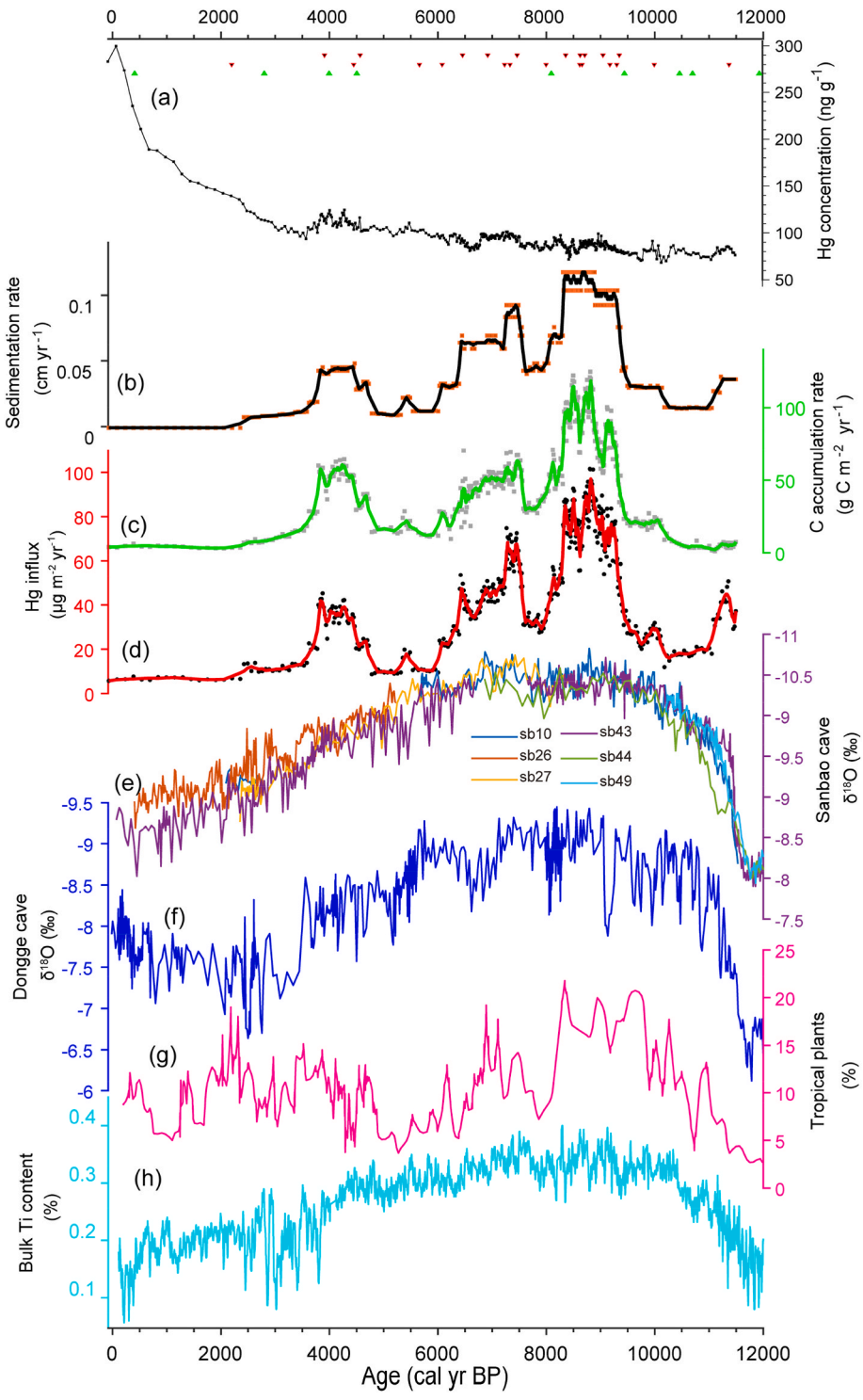

Fig. 3. Comparison of multi-parameter from Jiulongchi (a–d) and global climatic records (*d*–g) over the past 12,000 years. (a), (b), (c) and (d) are Hg concentrations (red solid triangles are AMS ^{14}C date control points from FJ19B (this study), green solid triangles are the dates from JL15 (Gao et al., 2019)), sedimentation rate, carbon accumulation rate, and Hg influx, respectively (brown, gray, and black circles reflect individual data points and solid lines are 5-point moving average). (e) Speleothem δ^{18}O records from Sanbao Cave (this record was derived from 6 pieces of stalagmites, which are shown in different colors) (Dong et al., 2010). (f) Speleothem δ^{18}O records from Dongge Cave (Dykoski et al., 2005). (g) Tropical plants pollen concentration records from Huguangyan Maar Lake (Wang et al., 2016). (h) Bulk Ti content of Cariaco Basin sediments from ODP Site 1002 (Haug et al., 2001). (For interpretation of the references to color in this figure legend, the reader is referred to the Web version of this article.)

4.2. Holocene Hg accumulation in jiulongchi

To elucidate the potential causes for higher Hg_{influx} in the pre-industrial period, we compared sedimentation rates and C accumulation rates with precipitations and climate data from the study area. Sedimentation rate and C accumulation at Jiulongchi also showed two peaks during the same periods of 10,000–6000 cal yr BP and 6000 - 3800 cal yr BP (Fig. 3b). The sedimentation rate of lacustrine deposits, particularly lakes with small or no catchment, is driven by precipitation intensities as there have no long-distance sediments transportation (Magny et al., 2013). In East Asia, Summer precipitation was mainly influenced by the intensity of the Asia Monsoon (AM) (Wang et al., 2005, 2016; Zhu et al., 2017). Thus, we expect that the intensified AM can lead to higher precipitation rates and increase soil runoff into lakes. As shown in Fig. 3, the Peak I of Hg_{influx} and sedimentation rates in Jiulongchi were associated with a strong AM from 9200 to 8200 cal yr BP, followed by a general weakening trend. This overall temporal pattern resembles the speleothem δ^{18}O data records from both central China (Dong et al., 2010), southwest China (Dykoski et al., 2005), the tropical plant pollen concentration data from the Huguangyan Maar

Lake in near the South China Sea (Wang et al., 2016), and the Ti concentration data from the Cariaco Basin in Tropical Atlantic (Haug et al., 2001) (Fig. 3e, f, g, and h). Speleothem $\delta^{18}O$ data from the selected sites are well-recognized proxies of Asian Monsoon intensity and Asian precipitation rates, where enriched speleothem $\delta^{18}O$ represent weak monsoon intensity and vice versa (Wang et al., 2005; Dong et al., 2010). As the Hg accumulation at Jiulongchi was driven by sedimentation rates, the association of Peak I of Hg_{influx} with more depleted $\delta^{18}O$ (Fig. 3) suggests that heavier precipitation first promoted higher sedimentation rates and then led to high Hg accumulation in Jiulongchi. The higher tropical plant pollen concentrations and Ti concentration data during this stage (Fig. 3g and h) all suggest a climatic optimum effect in the NH, which are responsible for the depleted speleothem $\delta^{18}O$ and peak sedimentation at Jiulongchi, during the occurrence of Hg_{influx} Peak I. Aside from climatic influences, it should be noted that volcanic activities could also contribute to the increases in Hginflux in sedimentary archives. The ice cores from Greenland have recorded several strong signals of volcano eruptions from 10,000–6000 cal yr BP (Zielinski et al., 1997). However, there is only one research from the Etang de la Gruère peat bog that has recorded several Hg concentration peaks accompanied by volcanic eruptions during this period (Roos-Barraclough et al., 2002). The volcanic Hg peak signals during the Holocene are absent in most studies (Jacobson et al., 2012; Li et al., 2016; Enrico et al., 2017; Pompeani et al., 2018; Schütze et al., 2018; Pan et al., 2020). More evidence from geological archives is needed to disentangle the effect of Holocene volcanic activities on global Hg cycling.

The Peak II of Hg_{influx} and sedimentation rates in Jiulongchi were interrupted by the sharp hydrological change corresponding to the mid-Holocene drought, which has been reported in various localities in China including the Dajiuhu Peat (Xie et al., 2013), Chenghai Lake (Xu et al., 2020), and Hongyuan Peat (Zheng et al., 2014). A recent study demonstrated that during the period from about 6000 to 3000 cal yr BP,

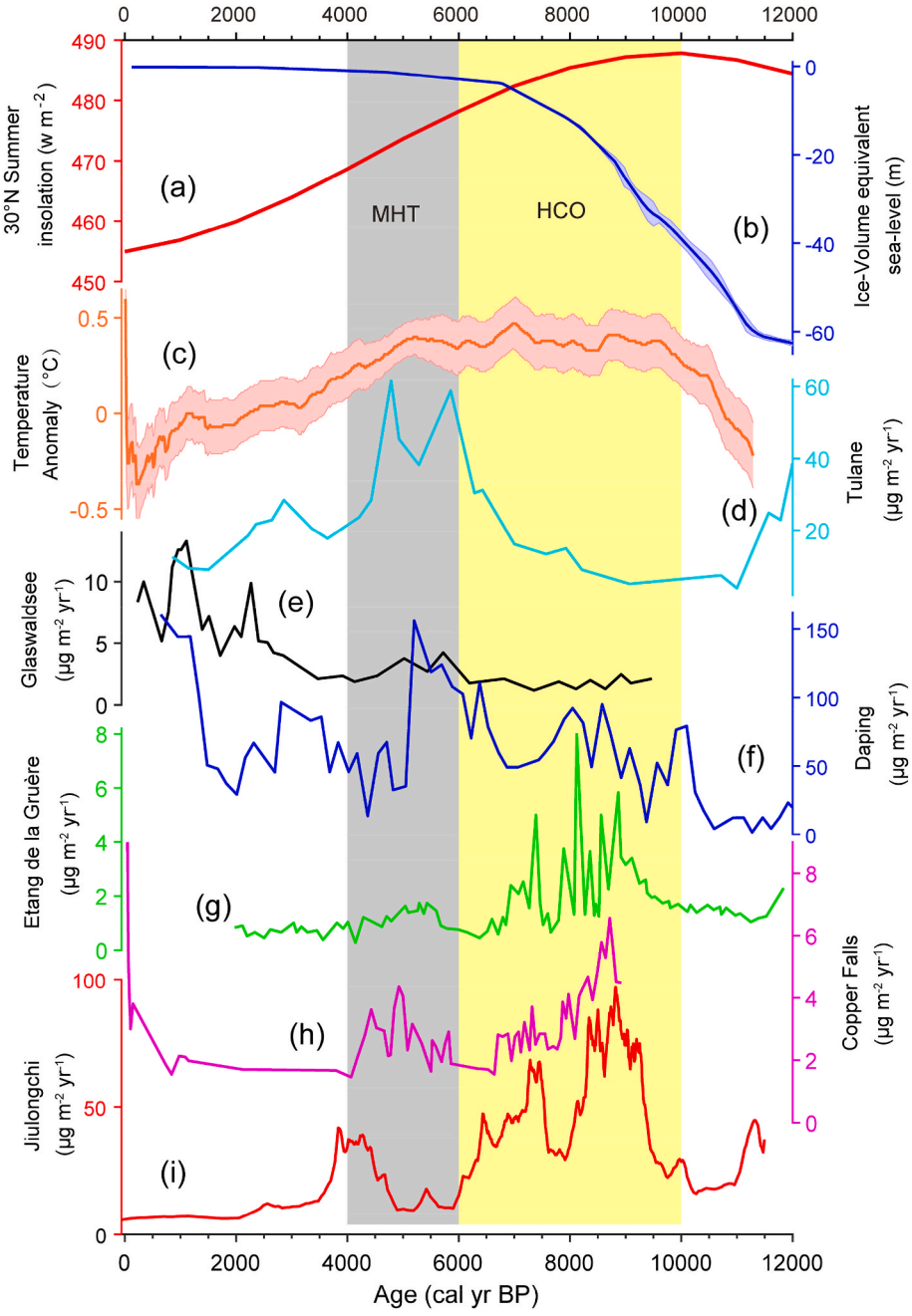

Fig. 4. Time series in **(a)** Holocene summer (June, July, and August) 30°N insolation (Berger and Loutre, 1991), **(b)** ice-volume equivalent sea-level (Lambeck et al., 2014), **(c)** global-scale temperature anomaly (Marcott et al., 2013), and Hg_{influx} of **(d)** Lake Tulane, USA (Jacobson et al., 2012), **(e)** Glaswaldsee, Germany (Schütze et al., 2018), **(f)** Daping Swamp, China (Pan et al., 2020), **(g)** Etang de la Gruère peatland, Switzerland (Roos-Barraclough et al., 2002), **(h)** Copper Falls Lake, USA (Pompeani et al., 2018), and **(i)** Jiulongchi wetland (this study).

strong/frequent storms and El Niño Southern Oscillation (ENSO) activities commonly occurred in central China (Zhu et al., 2017). During this period, decreased solar irradiance can weaken the AM, which in turn could cause location shifting of the Mei-yu Front, where tropical-subtropical warm-moist air meet the cooler continental air mass, and move southward to south China, thereby increasing the frequency of storms. Due to the increase in the amplitude of the ENSO (Wanner et al., 2008; Ward et al., 2014), the rebound in precipitation is expected to cause a rapid increase in both the sedimentation rate and thus Hg_{influx} (Fig. 3).

4.3. Holocene Hg accumulation in the northern hemisphere

The Earth's climate system is mainly driven by variations in solar insolation and the strength of the Atlantic Meridional Overturning Circulation (AMOC) on millennial time scales (Zhang, 2010; Corrick et al., 2020). The global climate has experienced several synchronous changes during the Holocene, such as the Holocene Climatic Optimum (HCO, ~10,000–6000 cal yr BP) (Baroni and Orombelli, 1996), the Mid-Holocene Transition (MHT, ~6000-4000 cal yr BP) (deMenocal et al., 2000), and the Neoglacial period (~4000 cal yr BP -present) (Porter and Denton, 1967). The two Hg_{influx} peaks observed in Jiulongchi coincide with those observed in globally distributed cores (Fig. 4). In contrast, THg concentrations in these cores showed only small temporal variations. This suggests that the occurrence of the two Hg_{influx} peaks was driven by intensified sedimentation rates, this further confirm what we found in the FJ19B core.

Peak I, observed in Jiulongchi and other three sites (Copper Falls Lake, Daping Swamp, Etang de la Gruère), coincides with the occurrence of HCO (~10,000–6000 yr BP) during which the summer insolation of the NH, the global average temperature, and the global sea surface temperature were the highest (Fig. 4a, b, c, f, g, h, and i). Driven by the higher insolation, rapid deglaciation happened in the NH high latitudes, resulting in global sea-level rise, which contributed more moisture to the atmospheric circulation (Denton et al., 2010; Stroeven et al., 2016). Coupling with the rising sea surface temperature and sea level, the northward migration of the ITCZ has caused more precipitation in the monsoon dominated areas in the NH (Haug et al., 2001; Wang et al., 2005). An increase in precipitation rates would have enhanced soil erosion, thereby the increased inputs of soil Hg to the lakes (Sonke et al., 2018; Jenny et al., 2019).

Peak II is observed at all sites and coincides roughly with the occurrence of the MHT (~6000-4000 cal yr BP) (Fig. 4). With the decline in NH summer insolation and the southward drifting of the ITCZ, the gradually intensified westerly jet and weakened AM have led to strong ENSO variability and less precipitation in the low-latitudes after the HCO (Haug et al., 2001; Wang et al., 2005; An et al., 2018). Notably, 5 abrupt drops in cosmogenic ^{14}C production rates happened during the MHT, which coincide with the mid-Holocene drought that was widely observed during this period (Stuiver et al., 1998; Staubwasser et al., 2003; Wang et al., 2005). After the drought, due to the increase in the amplitude of the ENSO (Wanner et al., 2008; Ward et al., 2014), the rebound in precipitation is expected to cause a rapid increase in both sedimentation rate and Hg_{influx}. We speculate that the abrupt changes in both solar radiation and ENSO variabilities during the MHT are the most important causes behind the Holocene Hg accumulation changes.

5. Conclusions

Based on large numbers of AMS^{14}C dates and Hg concentration analysis of a 450-cm long alpine wetland sediment core, we reconstructed the historical Hg influx of an alpine wetland during the Holocene in the southwest China Hg mining zone. Our record shows that the mining of the biggest Hg mine in China might have started 2500 years ago, which caused the doubling of Hg concentration in the alpine wetland since then. We found that pre-industrial Hg_{influx} is highly variable, and the variations are even greater than the increases caused by anthropogenic Hg releases. Besides, two Hg_{influx} peaks were observed during the Holocene Climatic Optimum and the Mid-Holocene Transition, which is similar in pattern to those recorded in other Northern Hemisphere sites. We speculate that critical climatic shifts, which could be ascribed to the migration of the ITCZ and fluctuations in the Asian monsoons during these periods, have led to the enhanced sedimentation and thus drove the two Hg_{influx} peaks. We contend that despite anthropogenic activities, global climate change would also have a significant effect on Hg deposition. Changes in climatic factors (e.g., temperature, monsoon intensity, and precipitation rates) can trigger sedimentation rates variations, which would also cause a large variation of Hg_{influx} in lake sediment on millennial timescales. Therefore, climate changes should also be taken into consideration to better quantify the discrepancies between modern and preindustrial Hg depositions.

Credit author statement

Haijun Peng: Conceptualization, Funding acquisition, Sampling, Writing – original draft. Yimeng Rong: Data Processing, Writing – original draft. Di Chen: Resources, Methodology. Ruiyang Sun: Resources. Jie Huang: Investigation, Methodology. Hanwei Ding: Resources, Investigation. Carolina Olid: Writing – review & editing, Methodology. Haiyu Yan: Writing – review & editing, Methodology. All authors discussed the results and contributed to the final manuscript.

Declaration of competing interest

The authors declare that they have no known competing financial interests or personal relationships that could have appeared to influence the work reported in this paper.

Data availability

Data will be made available on request.

References

An, S.I., Im, S.H., Jun, S.Y., 2018. Changes in ENSO activity during the last 6,000 Years modulated by background climate state. Geophys. Res. Lett. 45, 2467–2475.
Baroni, C., Orombelli, G., 1996. The Alpine ''iceman'' and holocene climatic change. Quat. Res. 46, 78–83.
Beal, S.A., Jackson, B.P., Kelly, M.A., Stroup, J.S., Landis, J.D., 2013. Effects of historical and modern mining on mercury deposition in southeastern Peru. Environ. Sci. Technol. 47, 12715–12720.
Beal, S.A., Kelly, M.A., Stroup, J.S., Jackson, B.P., Lowell, T.V., Tapia, P.M., 2014. Natural and anthropogenic variations in atmospheric mercury deposition during the Holocene near Quelccaya Ice Cap, Peru. Global Biogeochem. Cycles 28, 437–450.
Berger, A., Loutre, M.F., 1991. Insolation values for the climate of the last 10 million years. Quat. Sci. Rev. 10, 297–317.
Blaauw, M., Christen, J.A., 2011. Flexible paleoclimate age-depth models using an autoregressive gamma process. Bayesian analysis 6, 457–474.
Cheng, H., Sinha, A., Wang, X.F., Cruz, F.W., Edwards, R.L., 2012. The global paleomonsoon as seen through speleothem records from Asia and the americas. Clim. Dynam. 39, 1045–1062.
Cooke, C.A., Martínez-Cortizas, A., Bindler, R., Sexauer Gustin, M., 2020. Environmental archives of atmospheric Hg deposition – a review. Sci. Total Environ. 709, 134800.
Corrick, E.C., Drysdale, R.N., Hellstrom, J.C., Capron, E., Rasmussen, S.O., Zhang, X., Fleitmann, D., Couchoud, I., Wolff, E., 2020. Synchronous timing of abrupt climate changes during the last glacial period. Science 369, 963–969.
DahlJensen, D., Mosegaard, K., Gundestrup, N., Clow, G.D., Johnsen, S.J., Hansen, A.W., Balling, N., 1998. Past temperatures directly from the Greenland ice sheet. Science 282, 268–271.
deMenocal, P., Ortiz, J., Guilderson, T., Adkins, J., Sarnthein, M., Baker, L., Yarusinsky, M., 2000. Abrupt onset and termination of the African Humid Period: rapid climate responses to gradual insolation forcing. Quat. Sci. Rev. 19, 347–361.
Denton, G.H., Anderson, R.F., Toggweiler, J.R., Edwards, R.L., Schaefer, J.M., Putnam, A. E., 2010. The last glacial termination. Science 328, 1652–1656.
Díez, S., Esbrí, J.M., Tobias, A., Higueras, P., Martínez-Coronado, A., 2011. Determinants of exposure to mercury in hair from inhabitants of the largest mercury mine in the world. Chemosphere 84, 571–577.
Dong, J.G., Wang, Y.J., Cheng, H., Hardt, B., Edwards, R.L., Kong, X.G., Wu, J.Y., Chen, S.T., Liu, D.B., Jiang, X.Y., Zhao, K., 2010. A high-resolution stalagmite record

of the Holocene East Asian monsoon from Mt Shennongjia, central China. Holocene 20, 257–264.
Drevnick, P.E., Cooke, C.A., Barraza, D., Blais, J.M., Coale, K.H., Cumming, B.F., Curtis, C.J., Das, B., Donahue, W.F., Eagles-Smith, C.A., Engstrom, D.R., Fitzgerald, W.F., Furl, C.V., Gray, J.E., Hall, R.I., Jackson, T.A., Laird, K.R., Lockhart, W.L., Macdonald, R.W., Mast, M.A., Mathieu, C., Muir, D.C.G., Outridge, P. M., Reinemann, S.A., Rothenberg, S.E., Ruiz-Fernandez, A.C., St Louis, V.L., Sanders, R.D., Sanei, H., Skierszkan, E.K., Van Metre, P.C., Veverica, T.J., Wiklund, J.A., Wolfe, B.B., 2016. Spatiotemporal patterns of mercury accumulation in lake sediments of western North America. Sci. Total Environ. 568, 1157–1170.
Dykoski, C.A., Edwards, R.L., Cheng, H., Yuan, D.X., Cai, Y.J., Zhang, M.L., Lin, Y.S., Qing, J.M., An, Z.S., Revenaugh, J., 2005. A high-resolution, absolute-dated Holocene and deglacial Asian monsoon record from Dongge Cave, China. Earth Planet Sci. Lett. 233, 71–86.
Enrico, M., Le Roux, G., Heimbürger, L.-E., Van Beek, P., Souhaut, M., Chmeleff, J., Sonke, J.E., 2017. Holocene atmospheric mercury levels reconstructed from peat bog mercury stable isotopes. Environ. Sci. Technol. 51, 5899–5906.
Ernst, E., 2002. Toxic heavy metals and undeclared drugs in Asian herbal medicines. Trends Pharmacol. Sci. 23, 136–139.
Gao, Y., Xiong, K., Quan, M., Song, B., Peng, H., Peng, H., Shen, W., Bao, K., 2019. Holocene climate dynamics derived from pollen record of Jiulongchi wetland in Fanjing Mountain, southwest China. Quat. Int. 513, 1–7.
Grasby, S.E., Beauchamp, B., Bond, D.P.G., Wignall, P., Talavera, C., Galloway, J.M., Piepjohn, K., Reinhardt, L., Blomeier, D., 2015. Progressive environmental deterioration in northwestern Pangea leading to the latest Permian extinction. Geol. Soc. Am. Bull. 127, 1331–1347.
Grasby, S.E., Them, T.R., Chen, Z.H., Yin, R.S., Ardakani, O.H., 2019. Mercury as a proxy for volcanic emissions in the geologic record. Earth Sci. Rev. 196.
Grégoire, D.S., Poulain, A.J., Ivanova, E.P., 2018. Shining light on recent advances in microbial mercury cycling. FACETS 3, 858–879.
Haug, G.H., Hughen, K.A., Sigman, D.M., Peterson, L.C., Rohl, U., 2001. Southward migration of the intertropical convergence zone through the Holocene. Science 293, 1304–1308.
Hermanns, Y.M., Biester, H., 2013. A 17,300-year record of mercury accumulation in a pristine lake in southern Chile. J. Paleolimnol. 49, 547–561.
Jacobson, G.L., Norton, S.A., Grimm, E.C., Edgar, T., 2012. Changing climate and sea level alter Hg mobility at Lake Tulane, Florida, US. Environ. Sci. Technol. 46, 11710–11717.
Jenny, J.-P., Koirala, S., Gregory-Eaves, I., Francus, P., Niemann, C., Ahrens, B., Brovkin, V., Baud, A., Ojala, A.E.K., Normandeau, A., Zolitschka, B., Carvalhais, N., 2019. Human and climate global-scale imprint on sediment transfer during the Holocene. Proc. Natl. Acad. Sci. USA 116, 22972–22976.
Kaufman, D.S., Ager, T.A., Anderson, N.J., Anderson, P.M., Andrews, J.T., Bartlein, P.J., Brubaker, L.B., Coats, L.L., Cwynar, L.C., Duvall, M.L., Dyke, A.S., Edwards, M.E., Eisner, W.R., Gajewski, K., Geirsdottir, A., Hu, F.S., Jennings, A.E., Kaplan, M.R., Kerwin, M.N., Lozhkin, A.V., MacDonald, G.M., Miller, G.H., Mock, C.J., Oswald, W. W., Otto-Bliesner, B.L., Porinchu, D.F., Ruhland, K., Smol, J.P., Steig, E.J., Wolfe, B. B., 2004. Holocene thermal maximum in the western Arctic (0-180 degrees W). Quat. Sci. Rev. 23, 529–560.
Lambeck, K., Rouby, H., Purcell, A., Sun, Y.Y., Sambridge, M., 2014. sea level and global ice volumes from the last glacial maximum to the holocene. Proc. Natl. Acad. Sci. U. S.A. 111, 15296–15303.
Lamborg, C.H., Fitzgerald, W.F., Damman, A.W.H., Benoit, J.M., Balcom, P.H., Engstrom, D.R., 2002. Modern and historic atmospheric mercury fluxes in both hemispheres: global and regional mercury cycling implications. Global Biogeochem. Cycles 16.
Lepak, R.F., Janssen, S.E., Engstrom, D.R., Krabbenhoft, D.P., Tate, M.T., Yin, R., Fitzgerald, W.F., Nagorski, S.A., Hurley, J.P., 2020. Resolving atmospheric mercury loading and source trends from isotopic records of remote North American lake sediments. Environ. Sci. Technol. 54, 9325–9333.
Li, C., Sonke, J.E., Le Roux, G., Piotrowska, N., Van der Putten, N., Roberts, S.J., Daley, T., Rice, E., Gehrels, R., Enrico, M., Mauquoy, D., Roland, T.P., De Vleeschouwer, F., 2020a. Unequal anthropogenic enrichment of mercury in earth's northern and southern hemispheres. ACS Earth and Space Chem 4, 2073–2081.
Li, F., Ma, C., Zhang, P., 2020b. Mercury deposition, climate change and anthropogenic activities: a review. Front. Earth Sci. 8.
Li, P., Feng, X., Qiu, G., Zhang, J., Meng, B., Wang, J., 2013. Mercury speciation and mobility in mine wastes from mercury mines in China. Environ. Sci. Pollut. Control Ser. 20, 8374–8381.
Li, Y., Ma, C., Zhu, C., Huang, R., Zheng, C., 2016. Historical anthropogenic contributions to mercury accumulation recorded by a peat core from Dajiuhu montane mire, central China. Environ. Pollut. 216, 332–339.
Liao, H., Ren, M., 2015. Distribution patterns of long-lived individuals of relict plants around Fanjingshan Mountain in China: implications for in situ conservation. Collect. Bot. 34, e002.
Magny, M., Leroux, A., Bichet, V., Gauthier, E., Richard, H., Walter-Simonnet, A.-V., 2013. Climate, vegetation and land use as drivers of Holocene sedimentation: a case study from Lake Saint-Point (Jura Mountains, eastern France). Holocene 23, 137–147.
Marcott, S.A., Shakun, J.D., Clark, P.U., Mix, A.C., 2013. A reconstruction of regional and global temperature for the past 11,300 years. Science 339, 1198–1201.
Martínez-Cortizas, A., Pontevedra-Pombal, X., García-Rodeja, E., Nóvoa-Muñoz, J.C., Shotyk, W., 1999. Mercury in a Spanish peat bog: archive of climate change and atmospheric metal deposition. Science 284, 939–942.
Neupane, B., Bao, K., Chen, M., Thapa, P., Meadows, M.E., 2022. The timing and magnitude of anthropogenic mercury pollution: a 200-year record from multi-lake sediment cores in northeast China. Chemosphere 309, 136803.
Obrist, D., Kirk, J.L., Zhang, L., Sunderland, E.M., Jiskra, M., Selin, N.E., 2018. A review of global environmental mercury processes in response to human and natural perturbations: changes of emissions, climate, and land use. Ambio 47, 116–140.
Pan, J.Y., Zhong, W., Wei, Z.Q., Ouyang, J., Shang, S.T., Ye, S.S., Chen, Y.H., Xue, J.B., Tang, X.W., 2020. A 15,400-year record of natural and anthropogenic input of mercury (Hg) in a sub-alpine lacustrine sediment succession from the western Nanling Mountains, South China. Environ. Sci. Pollut. Control Ser. 27, 20478–20489.
Pompeani, D.P., Cooke, C.A., Abbott, M.B., Drevnick, P.E., 2018. Climate, fire, and vegetation mediate mercury delivery to midlatitude lakes over the holocene. Environ. Sci. Technol. 52, 8157–8164.
Porter, S.C., Denton, G.H., 1967. Chronology of neoglaciation in the North American cordillera. Am. J. Sci. 265, 177–210.
Reimer, P.J., Bard, E., Bayliss, A., Beck, J.W., Blackwell, P.G., Ramsey, C.B., Buck, C.E., Cheng, H., Edwards, R.L., Friedrich, M., Grootes, P.M., Guilderson, T.P., Haflidason, H., Hajdas, I., Hatté, C., Heaton, T.J., Hoffmann, D.L., Hogg, A.G., Hughen, K.A., Kaiser, K.F., Kromer, B., Manning, S.W., Niu, M., Reimer, R.W., Richards, D.A., Scott, E.M., Southon, J.R., Staff, R.A., Turney, C.S.M., van der Plicht, J., 2013. IntCal13 and Marine13 radiocarbon age calibration curves 0–50,000 Years cal BP. Radiocarbon 55, 1869–1887.
Rong, Y., Peng, H., Ding, H., Bao, K., Gao, Y., Yan, H., Di, C., Hu, Y., Jie, W., 2021. A study on the ^{14}C chronology of Jiulongchi wetland deposit on the Fanjingshan Mountain and its carbon accumulation rate during the Holocene. Earth Environ. 1–11 (in Chinese with English abstract).
Roos-Barraclough, F., Martinez-Cortizas, A., Garcia-Rodeja, E., Shotyk, W., 2002. A 14 500 year record of the accumulation of atmospheric mercury in peat: volcanic signals, anthropogenic influences and a correlation to bromine accumulation. Earth Planet Sci. Lett. 202, 435–451.
Schütze, M., Tserendorj, G., Pérez-Rodríguez, M., Rösch, M., Biester, H., 2018. Prediction of holocene mercury accumulation trends by combining palynological and geochemical records of lake sediments (black forest, Germany). Geosciences 8, 358.
Selin, N.E., 2009. Global biogeochemical cycling of mercury: a review. Annu. Rev. Environ. Resour. 34, 43–63.
Sonke, J.E., Teisserenc, R., Heimbürger-Boavida, L.-E., Petrova, M.V., Marusczak, N., Le Dantec, T., Chupakov, A.V., Li, C., Thackray, C.P., Sunderland, E.M., Tananaev, N., Pokrovsky, O.S., 2018. Eurasian river spring flood observations support net Arctic Ocean mercury export to the atmosphere and Atlantic Ocean. Proc. Natl. Acad. Sci. USA 115, E11586–E11594.
Staubwasser, M., Sirocko, F., Grootes, P.M., Segl, M., 2003. Climate change at the 4.2 ka BP termination of the Indus valley civilization and Holocene south Asian monsoon variability. Geophys. Res. Lett. 30.
Stroeven, A.P., Hättestrand, C., Kleman, J., Heyman, J., Fabel, D., Fredin, O., Goodfellow, B.W., Harbor, J.M., Jansen, J.D., Olsen, L., Caffee, M.W., Fink, D., Lundqvist, J., Rosqvist, G.C., Strömberg, B., Jansson, K.N., 2016. Deglaciation of fennoscandia. Quat. Sci. Rev. 147, 91–121.
Stuiver, M., Reimer, P.J., Bard, E., Beck, J.W., Burr, G.S., Hughen, K.A., Kromer, B., McCormac, G., Van Der Plicht, J., Spurk, M., 1998. INTCAL98 radiocarbon age calibration, 24,000–0 cal BP. Radiocarbon 40, 1041–1083.
Walkley, A., 1947. A critical examination of a rapid method for determining organic carbon in soils. Effects of variations in digestion conditions and of inorganic soil sonstituents. Soil Sci. 63, 251–264.
Wang, B., Zhong, S., Bishop, K., Nilsson, M.B., Hu, H., Eklöf, K., Bravo, A.G., Åkerblom, S., Bertilsson, S., Björn, E., Skyllberg, U., 2021. Biogeochemical influences on net methylmercury formation proxies along a peatland chronosequence. Geochem. Cosmochim. Acta 308, 188–203.
Wang, X.S., Chu, G.Q., Sheng, M., Zhang, S.Q., Li, J.H., Chen, Y., Tang, L., Su, Y.L., Pei, J. L., Yang, Z.Y., 2016. Millennial-scale Asian summer monsoon variations in South China since the last deglaciation. Earth Planet Sci. Lett. 451, 22–30.
Wang, Y.J., Cheng, H., Edwards, R.L., He, Y.Q., Kong, X.G., An, Z.S., Wu, J.Y., Kelly, M. J., Dykoski, C.A., Li, X.D., 2005. The holocene asian monsoon: links to solar changes and North atlantic climate. Science 308, 854–857.
Wanner, H., Beer, J., Butikofer, J., Crowley, T.J., Cubasch, U., Fluckiger, J., Goosse, H., Grosjean, M., Joos, F., Kaplan, J.O., Kuttel, M., Muller, S.A., Prentice, I.C., Solomina, O., Stocker, T.F., Tarasov, P., Wagner, M., Widmann, M., 2008. Mid- to Late Holocene climate change: an overview. Quat. Sci. Rev. 27, 1791–1828.
Ward, P.J., Jongman, B., Kummu, M., Dettinger, M.D., Weiland, F.C.S., Winsemius, H.C., 2014. Strong influence of El Niño Southern Oscillation on flood risk around the world. Proc. Natl. Acad. Sci. U.S.A. 111, 15659–15664.
Xie, S.C., Evershed, R.P., Huang, X.Y., Zhu, Z.M., Pancost, R.D., Meyers, P.A., Gong, L.F., Hu, C.Y., Huang, J.H., Zhang, S.H., Gu, Y.S., Zhu, J.Y., 2013. Concordant monsoon-driven postglacial hydrological changes in peat and stalagmite records and their impacts on prehistoric cultures in central China. Geology 41, 827–830.
Xiong, G., Duan, T., Wu, H., Zhang, H., Yu, Q., Yan, J., Jiang, X., Cui, X., Wang, J., Wang, Z., 2013. Carbon and oxygen isotopic characteristics of the ediacaran doushantuo formation in fanjingshan area, northeastern Guizhou province, China. Carbonates Evaporites 28, 399–412.
Xu, H., Goldsmith, Y., Lan, J.H., Tan, L.C., Wang, X.L., Zhou, X.Y., Cheng, J., Lang, Y.C., Liu, C.Q., 2020. Juxtaposition of western pacific subtropical high on asian summer monsoon shapes subtropical east asian precipitation. Geophys. Res. Lett. 47.
Yin, R., Feng, X., Hurley, J.P., Krabbenhoft, D.P., Lepak, R.F., Kang, S., Yang, H., Li, X., 2016. Historical records of mercury stable isotopes in sediments of Tibetan lakes. Sci. Rep. 6, 23332.

Yin, R., Feng, X., Wang, J., Bao, Z., Yu, B., Chen, J., 2013. Mercury isotope variations between bioavailable mercury fractions and total mercury in mercury contaminated soil in Wanshan Mercury Mine, SW China. Chem. Geol. 336, 80–86.
Yin, R., Zhang, W., Sun, G., Feng, Z., Hurley, J.P., Yang, L., Shang, L., Feng, X., 2017. Mercury risk in poultry in the wanshan mercury mine, China. Environ. Pollut. 230, 810–816.
Zhang, H., Feng, X., Larssen, T., Shang, L., Vogt, R.D., Rothenberg, S.E., Li, P., Zhang, H., Lin, Y., 2010. Fractionation, distribution and transport of mercury in rivers and tributaries around Wanshan Hg mining district, Guizhou province, southwestern China: Part 1 – total mercury. Appl. Geochem. 25, 633–641.
Zhang, H., Yin, R.-s., Feng, X.-b., Sommar, J., Anderson, C.W.N., Sapkota, A., Fu, X.-w., Larssen, T., 2013. Atmospheric mercury inputs in montane soils increase with elevation: evidence from mercury isotope signatures. Sci. Rep. 3, 3322.
Zhang, R., 2010. Latitudinal dependence of Atlantic meridional overturning circulation (AMOC) variations. Geophys. Res. Lett. 37.
Zheng, Y.H., Singarayer, J.S., Cheng, P., Yu, X.F., Liu, Z., Valdes, P.J., Pancost, R.D., 2014. Holocene variations in peatland methane cycling associated with the Asian summer monsoon system. Nat. Commun. 5.
Zhu, Z.M., Feinberg, J.M., Xie, S.C., Bourne, M.D., Huang, C.J., Hu, C.Y., Cheng, H., 2017. Holocene ENSO-related cyclic storms recorded by magnetic minerals in speleothems of central China. Proc. Natl. Acad. Sci. U.S.A. 114, 852–857.
Zielinski, G.A., Mayewski, P.A., Meeker, L.D., Grönvold, K., Germani, M.S., Whitlow, S., Twickler, M.S., Taylor, K., 1997. Volcanic aerosol records and tephrochronology of the Summit, Greenland, ice cores. J. Geophys. Res.: Oceans 102, 26625–26640.